Journal of Applied Fluid Mechanics, Vol. 16, No. 12, pp. 2344-2363, 2023.
Available online at www.jafmonline.net, ISSN 1735-3572, EISSN 1735-3645.
https://doi.org/10.47176/jafm.16.12.2032

Aerodynamic and RSM Analysis of Wingsuit Stability

M. Nazemian Alaei† and M. S. Valipour

Faculty of Mechanical Engineering, Semnan University, Semnan, Iran

†*Corresponding author E-mail: mohsen.nazemian@semnan.ac.ir*

ABSTRACT

A Wingsuit is a Skydiving Jumpsuit that generates more lift for longer flights. This study examined the effects of side slip angles on a beginner wingsuit at 10^6 Reynolds number. Experimental tests were determined by using the length of the model scale at angles of attack ranging from 0° to 40° and sideslip angles of up to 20°. Force and moment coefficients were analyzed using variations in angles of attack and sideslip. Despite the absence of significant effects of sideslip angles on the lift and drag coefficients, side force and rolling/yawing moments were highly nonlinear. Flow structure visualization and numerical simulation show that surface stalls only occur on the lower side when slip angles are lower. In individual aviation sports, wingsuits are more advantageous when they have less sideslip. With Tuft visualization on the wingsuit model, the best aerodynamic coefficient under different flight conditions was determined by comparing the Response Surface Methodology performance under different flight conditions.

Article History

Received May 22, 2023
Revised July 4, 2023
Accepted July 27, 2023
Available online October 8, 2023

Keywords:

Wingsuit
Lateral Stability
Response surface methodology (RSM)
Tuft flow visualization

1. INTRODUCTION

A wingsuit can be defined as a wearable suit manufactured with special fabrics that enables the user to fly, after jumping off of a high cliff, a bridge, out of an airplane, or similar environment. The modern wingsuit, first developed in the late 1990s, adds surface area with fabric between the legs and under the arms of the pilot, which functions in a similar manner to aircraft wings, in order to increase the lift acting on the human body during flight (Fig. 1). This configuration is often called the tri-wing wingsuit. The "wings" are designed to be ram-air inflated in order to achieve more rigid wing structures and airfoil shapes along cross-sections, leading to better aerodynamic performance.

The material used in wingsuits are commonly nylon (100% polyamide), taslan (100% polyester), belga (65% polyester 35% cotton, and polycotton (60% polyester, 40% cotton) (Kornilovich & Kuzmichev, 2016). Different materials have different weights and strengths, as well as various drag resistances when flying through air. Therefore they are used according to flight conditions such as slow, normal and fast speeds (Stockl et al., 2020).

Wingsuit operators play an extremely important role in the wingsuit, which is supported by numerous jumping experiences. In any case, the location of the air inlets should not adversely affect wearing comfort. Wings or suits are integrated with air chambers. Inflating them, keeping the air inside, and thus creating a semi-rigid wing shape, are their main functions. It is not possible to reduce landing speed sufficiently without additional tools if the wings are too small. A parachute is therefore necessary. The parachute bags are filled with a main and a reserve parachute (Sieker et al., 2019).

Aerodynamics play an important role in high-performance sports activities. Wearing an aerodynamically appropriate outfit can considerably improve the functionality of the athlete. Profound knowledge regarding aerodynamic effects on material behavior and product shape helps to improve the desired aspects and avoid mistakes. Recent research has shown progress in athletes' performance by using high-performance sportswear (Ishikura et al., 2014; Hayes & Venkatraman, 2018).

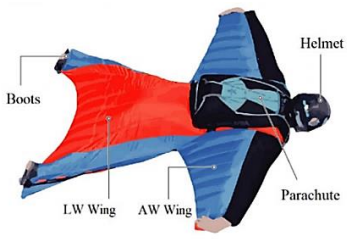

Fig. 1 Beginner level wingsuit with ram-air inflated

NOMENCLATURE

Symbols

AOA	angle of attack
C_D	drag coefficient
D	drag force
V	free velocity
C_L	lift coefficient
C_Y	side force coefficient
C_m	pitching moment coefficient
C_n	yawing moment coefficient
C_l	rolling moment coefficient
L	lift force
L_m	length of the wingsuit
L/D	aerodynamics efficiency (lift-to-drag ratio)
RC	coefficient responses
Re	Reynolds number
h_m	wave domain
n	number of ridges on HW
β	side angle
λ	wave scale
L_H	length of the arm of wingsuit

Abbreviations

AR	Aspect Ratio
HW	Wing of Hand
LW	Wing of Leg
GR	Glide Ratio (height/distance)
CG	Center of Gravity
CFD	Computational Fluid Dynamics

wingsuit can reduce these speeds dramatically. A vertical instantaneous velocity of 40 km/h (25 mph) has been recorded. However, the speed at which the body advances forward through the air is still high, up to 100 km/h (62 mph). A regular wingsuit flight where a pilot jumps out of an airplane usually begins at 4,000 m (13,000 ft.) and the pilot spends one to two minutes in free fall before drifting gently to Earth. In this case, the horizontal gliding distance is around 10,000 m (32,500 ft.). This wingsuit flight allows the pilot to achieve glide ratios of approximately 2.5 (2,500 m of horizontal travel for every 1,000 m of vertical descent). A wingsuit pilot must consider each of the three parameters: lift, drag, and glide ratio. It is generally preferred to increase glide ratio for long-range flights, increase lift force for increasing fall time, and decrease drag force for increasing forward speed. In addition to the glide radio and the maneuverability of the wingsuit, stability is an important factor to wingsuit pilots. In comparison, hang gliders fly with a glide ratio of 15. Space shuttles approach Earth with a glide ratio of 4.5 (Zhang, 2016). Northern flying squirrels achieve glide ratios of at most 2.0. For wingsuit flight, the record of the largest glide ratio of 4 can be achieved by the highly skilled skydiver wearing a high-performance wingsuit (Omholt, 2011).

Recent developments in the wingsuit industry have led to wingsuit designs that are not just visually appealing, but are also more efficient (Stockl et al., 2020). In order to improve aerodynamic characteristics, unconventional designs are introduced. A wing's shape is one of them. By providing stability and control, the wingsuit is able to recover from perturbations in pitch, yaw, and roll. In order to maintain body control during various disturbances, it is vital that the wingsuit is stable (Zhang, 2016). While aerodynamicists believe that wings add structural weight and wetted area, they are often sized with as few changes as possible. The wing surface is generally sized based on the required aerodynamic and control forces, although in some cases this is not optimal (Ansari et al., 2018). Consequently, many unconventional wingsuit configurations have been developed, with hand-foot wings that provide both lateral stability and directional control. This design was introduced in 1912 by Reichelt, but was grounded due to safety concerns (Robson & D'Andrea, 2010). At this moment, lots of wingsuits use textile as it provides fascinating features (Abrams, 2007). There are a variety of wingsuit configurations available for different operations and missions today due to the growing popularity of aviation sports and scientific research (Feletti et al., 2017). It is critical that wingsuits are designed with a high lift-to-drag ratio and a low induce drag criterion to satisfy the requirement of long-endurance flight.

Pilots have complained about the difficulty in flying the wingsuit to parachutist release because materials for best-glide ratio (GR) are required in the model (Sestak, 2017). Additionally, there are many cases of pilots complaining about the difficulty of flying wingsuit parachutists (Kornilovich, 2017). A number of fatal accidents have occurred due to loss of control of the Parachute Release system, particularly when flying laterally. Flying and handling problems, especially when in Dutch roll mode, may occur with wingsuits that have an informal posture (Ansari, 2019). In gusty conditions, the wingsuit may be exacerbated by these problems, as the flow around it plays a crucial role in stabilizing and securing it (Sieker et al., 2019).

A geometrical change on a surface can be considered a passive controller according to aerodynamic theory (Ozkan, 2022). As a result, geometrical changes play an important role in the flight performance of bird models (Jacob et al., 2007; Dvořák, 2016), including wingsuits. A significant characteristic of inflatable wings is the wave shape geometry, which we examined in relation to aerodynamic forces, moments, and flow structure in this study using a wingsuit model. It is possible for beginners' wingsuits to have wavy surfaces, which can have positive or negative effects depending on how they are positioned (Alaei & Valipour, 2023). Therefore, this study examines the performance and flight control of a wingsuit with wavy ridges placed on it. In order to better understand the subject, a rigid model was chosen for the study. Using Tufts visualization and numerical simulation, we were able to observe the flow structure on the surface of the wingsuit model in the scale of the experiment model. Tufts examined the disturbed area to visualize the flow at different angles of attack (AOAs) and side angles (β).

A beginner wingsuit geometry was simulated under symmetrical conditions in a steady state. The investigations were not designed to optimize or extract precise values. It is a relatively simple model that aims to

determine whether the wingsuit can fly stable due to its generic shape. In spite of its difference in width from the real wingsuit, this simple geometry construction still helps to describe the aerodynamic behavior of the wingsuit, for example, the helmet, parachute, and other body parts.

This study focused on reduced-scaled wingsuits to acquire aerodynamic characteristics from wind tunnel tests. The Model Development Steps included the design, modification, and Manufacturing of the beginner-level wingsuit model. The model was tested in the wind tunnel at various angles of attack and sideslip angles. The model was designed to fulfill the basic flying techniques and aerobatic moves during wingsuit real flights. This wingsuit model applied the aerodynamic coefficients of the wingsuit model to a pilot with a full-size commercial wingsuit. The results show that the wingsuit is a highly maneuverable flight. Finally, the stability was analyzed of its modes of for variation side angles. In addition, the results of simulations and experimental analysis feedback in the design of the beginner surface of the wingsuit model showed that the change in the lateral angle of flight can reduce the control and stability so that at AOA=10° with the smallest body angle (β=5°) relative to the direction of the flow, the rolling moment coefficient is increased to 2.3 times and the L/D value decreases to 14%.

2. EXPERIMENTAL DETAILS

Wind tunnel studies provide data for aerodynamic force and moment as a function of the athlete's posture, the angle of attack, the shape of the model, and the product shape. Choosing the model with the best scale for experiments in a wind tunnel is the first step to achieving the most realistic results. Parameters such as correct intensity and homogenous velocity of airflow are influencing variables by wind tunnel setup that are considered in this study. For this study, first, the experimental data obtained by the wind tunnel study of the wingsuit model are presented. Second, the data and contour plots for the CFD simulation of the wingsuit model are presented and compared with the experimental data. Finally, graphs of key variables for the wingsuit model are compared.

2.1 Wind Tunnel Testing Facilities

Figure 2 shows the experimental set-up consisting of 1.2m wide, 1m high, and 3m long rectangular open-circuit wind tunnels. Non-uniformity of velocity across the test section was within +0.5%, and turbulence intensity of the longitudinal free-stream was below 0.15%. First, the equipment and relevant software for measuring airflow specifications were used to measure speeds and static pressures. The resulting data of these measurements were analyzed. Also, calibration of the balancing device for different weights was individually done. The wind tunnel facility for this study is shown in Fig. 2.

In order to conduct the simulation of the flight dynamics of the wingsuit model, aerodynamic coefficients must be calculated from the wind tunnel tests data, such as lift force, drag force, side force, as well as moments along each axis. First, an aluminum holder was designed. On one end of the holder, it was mounted tightly with set screws

(a)

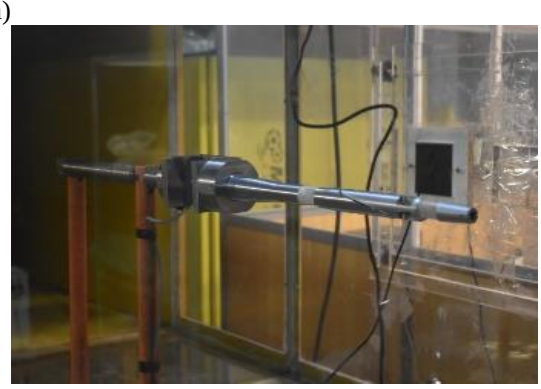

(b)

Fig. 2 Experimental facility (a) Wind tunnel (b) The adjustment mechanism of the AOA and balance

onto the strain gauge of the balance. And on the other end, it connected to an iron rod that was fixed in the human body model. Eventually, the wingsuit model was connected to the strain gauge for the purpose of data acquisition, as shown in Fig. 2.

There were six sets of data obtained from wind tunnel tests, which are axial force, side force, normal force, roll moment, pitch moment, and yaw moment along x, y, and z-axis respectively. Note that all the forces and moments were given in the body frame of the balance. After the data was exported from the wind tunnel data logger, all the forces and moments were transferred from the balance body frame to the wind frame. The distance between the wind tunnel balance measurement point and the center of gravity of the wingsuit model was measured and used in the calculation of pitching moment. Meaning that the pitching moment of the wingsuit model was calculated relative to its center of gravity.

2.2 Parametric Geometry Model Design

Experiment tests were done in velocity at 30 (m/s) at ten AOAs for assessment and measurement of the force and flow structure. The wingsuit had a two-surface wing (HW) and wing between of leg (LW) with a chord-wise airfoil wing section. A trapezoidal wing was controlled by the flyer by changing its dihedral and anhedral. By sweeping the wing aft, slack was created in the wing material, which allowed the material to billow upward and reduce the rigidity of the airfoil shape (Feletti et al., 2017).

A smooth, polished, painted wing surface was used as a baseline for the comparison of the upper surfaces with various wave-shaped structures which were created

Table 1 Geometric Parameters of the Wingsuit

Model label	Geometric of model			Geometric Properties of Wave on Top of HW and LW				
	AR	*span*	*length*	*n*	$\lambda\ (cm)$	$h_m\ (cm)$	h_m/L_H	λ/L_H
Wingsuit Model (WMN7)	2.22	0.6	0.7	7	3.28	0.44	0.02	0.14

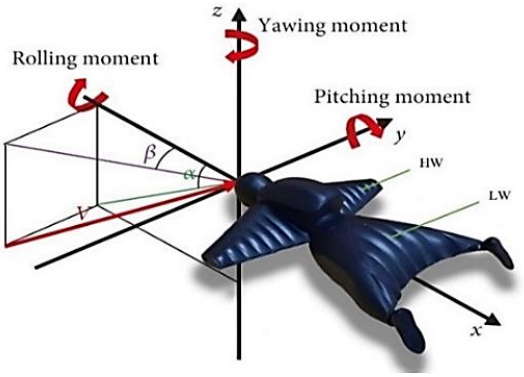

Fig. 3 Systems of coordinates and sign conventions for moment coefficients

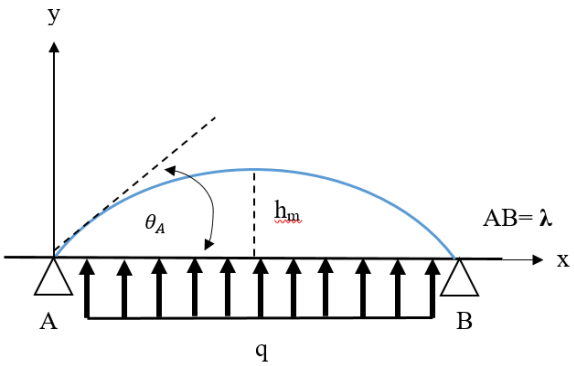

Fig. 4 Load distribution on a simply support

during the flight on the wing clothing. Figure 3 shows these three configurations with coordinate system in flight.

A catenary was assumed to form the surface of the suit, as shown in Fig. 4. The spacing between two ribs was set to 32,8 mm for this model. Hence, in 2D, the model surface similar to the suit in 2D can be calculated by Eq. (1) as a simply supported beam subject to uniform pressure load (Merkin, 1980).

$$y(x) = \theta_A \times \frac{x}{L^3}(x^3 - 2Lx^2 + L^3) \quad (1)$$

According to the information provided by a wingsuit manufacturer, θ_A is estimated to be between 30◦ and 35◦ for such a rib spacing to chord ratio. Based on the internal pressure equation used in the textile sewing of this suit, the investigations were conducted for the developed wingsuit geometries (Table 1).

The AOAs, defined by the angle of the supporting device in the experiments, were AOA= 0° to AOA=40°. Re was 1.3×10^6, and the Mach number was at a maximum of 0.1 for all test cases. Wingsuit model blockage ratio were 4.1% at AOA=0° and 10.4% at AOA=30°. It is

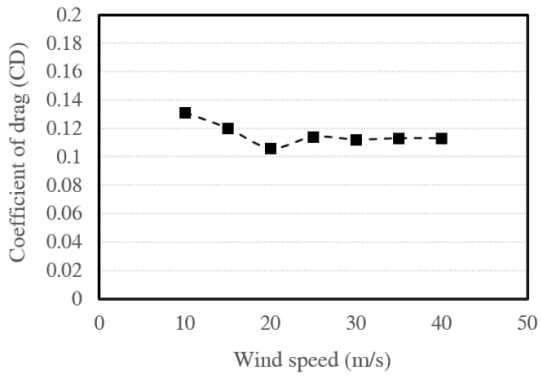

Fig. 5 Variation in drag coefficient with wind speed in Reynolds sweep tests

recommended not to exceed 10% for the frontal section to the test section. (Barlow et al., 1999).

2.3. Experimental Results and Discussions

2.3.1. Reynolds Sweep Test

Results are presented here based on the CG of the wingsuits, with force and moment results related to lateral stability being presented as body axis data. In this study, wind tunnel testing was used to measure aerodynamic characteristics and mini-tuft visualization was used to predict vortex structure. The configuration of the wingsuit model for the training brigade was tested in the wind tunnel at a speed of 30 m/s for different side slip angles of 5°, 10°, and 20°. Various wind speeds were tested at zero attack and zero yaw angles in Reynolds sweep tests to determine the appropriate test speed. The drag coefficient is then evaluated to determine at which wind speeds it is independent of the wind speed. In Fig. 5, we illustrate the results of the Reynolds sweep at wind speeds of 10 m/s to 40 m/s, where the drag coefficients are almost identical at 30 m/s and above. This consideration should be taken into consideration when making the choice. Hence, a wind speed of 30m/s which corresponds to the Reynolds number of 1.3×10^6 based on the model length (0.7m) was selected to be a test.

2.3.2. Flow Visualization

By using mini-tuft flow visualizations are performed. As part of the visualizations of mini tufts flows, 25 mm long ad 2 mm diameter stockinet yarns were attached to the model's upper surface. These yarns allowed us to identify mini tufts aligned with flow and/or with reversal movements indicating clearly regions of attacked and detached flow.

The experiments were performed at different AOAs have been varied from AOA=0° to AOA=40° in

increments of five degrees. Through the tuft, flow patterns on the surfaces of HW and LW were detected, and the force balance gives the lift, drag, and pitching moment. In comparison with the wingtip, a higher rate of disturbance was observed near the center of the wing. This was attributed to the wing's spanwise flow. The tufts on the wing showed any motion at AOA=10° and AOA=35° at β=0°, but there was a slight movement at the trailing edge. At this point, the flow is beginning to separate. The airflow was reversed around the trailing edge from AOA=10° onward. At this angle of attack, the tuft flow reversal was very significant. The AOA increases by 5 degrees while keeping the model in the center of the test section, as shown in Figs. (6,7).

Wingsuit drag and lift coefficients are also calculated. The streamlines of velocity around a wingsuit for HW and LW wings for various angles of attack can be seen in Figs. (6,7), and the produced spanwise vortex is stronger and positioned on the rear of the backpack. In the chord length region, a chordwise vortex forms, and its attachment and separation lines are close in proximity to the TE of the

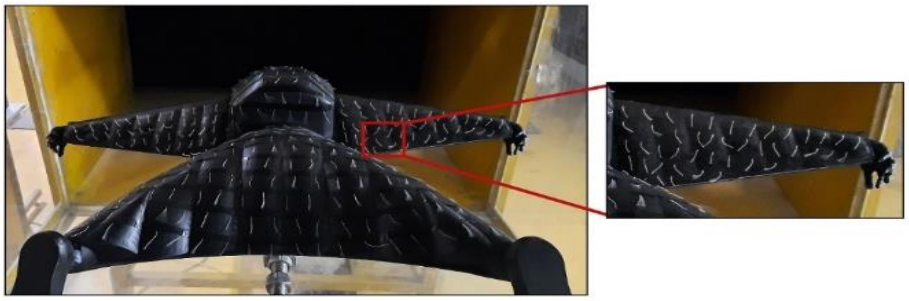

(a) AOA=10°

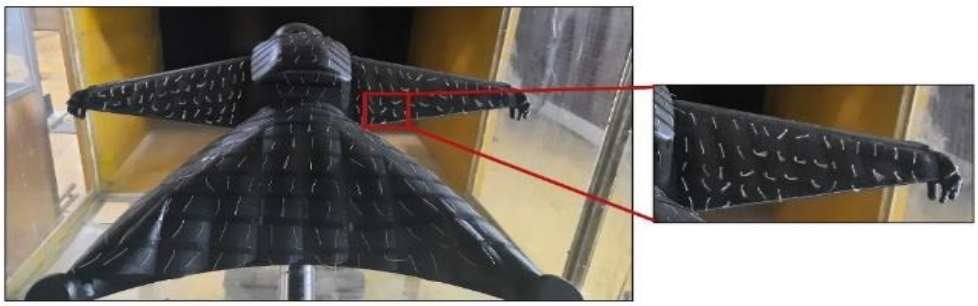

(b) AOA=35°

Fig. 6 Flow visualization with mini tuft on wingsuit models at different AOAs and β=0° at Re≈ 1.3×10^6

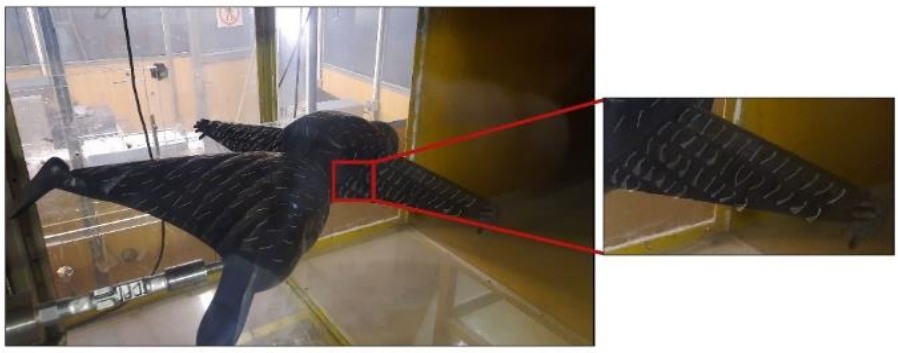

(a) AOA=10°

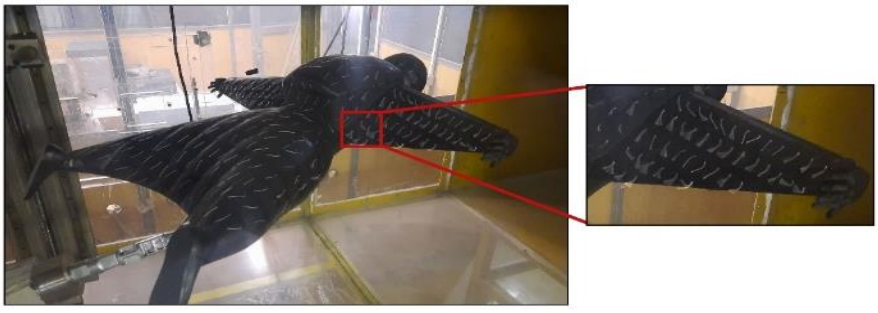

(b) AOA=35°

Fig. 7 Flow visualization with mini tuft on wingsuit models at different AOAs and β=15° at Re≈ 1.3×10^6

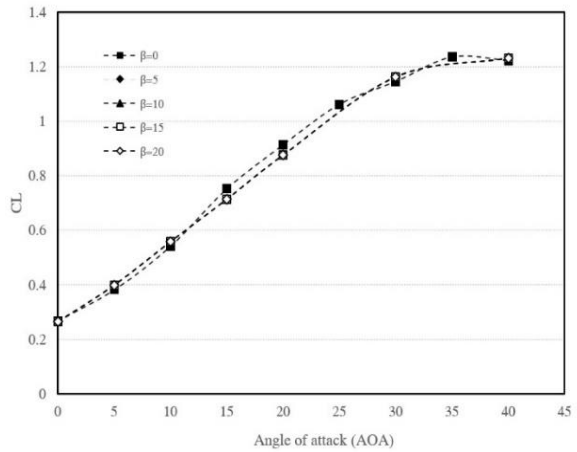

(a) Lift coefficient

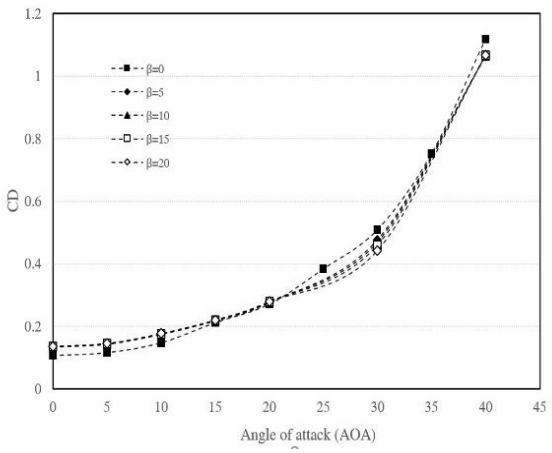

(b) Drag coefficient

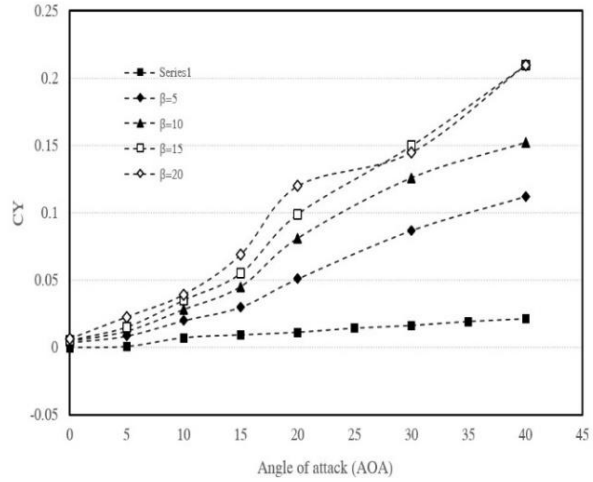

(c) Side force coefficient

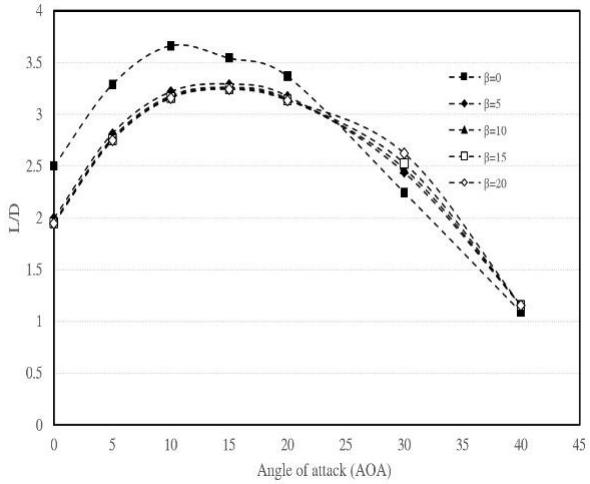

(d) Lift-to-drag ratio (L/D)

Fig. 8 Analysis of lift, drag, side force coefficients and Lift-to-drag ratio (L/D) for different AOAs and β at Re≈1.3×106

wing. Furthermore, the presence of primary and secondary LE (outer) counter-rotating vortices can be detected. Most of the test conditions are accompanied by the onset of the primary vortex, especially for the HW wing. By looking at streamlines, secondary vortices were not detected. In the streamlined pictures, you can see where the primary and secondary vortexes are separated and attached. The streamlines to vortex breakdown around the rear edges of the legs are shown in Figs. (6,7). Both HW for all AOAs were able to see the development of the primary vortex. Vortex generation usually occurs earlier on wavy ridges geometry.

In all the experiments, the Reynolds number of 1.3×10^6. We have done experiments in five-degree intervals from AOA=0° to AOA=40°. Through balance system measurements, flow structures were detected on the up surface of HW and LW, and Drag and Lift aerodynamic forces and moments were measured. Analyzing the values from the experiments, the stall in the model of the wingsuit was evaluated. The force sensors in the system with sensors were first used to measure the forces, and their output was obtained by the data acquisition card, which is capable of acquiring the force sensor data from the balance device and transmitting it directly into the computer via an interface that is easily accessible by a processing card.

2.3.3. Force and Moment Measurement

For the wingsuit pilot to obtain terminal velocity, the wingsuit has to generate a certain amount of lift. Fig. 8 shows for which angles of attack this happens.

We can investigate the lift parameter by the experiment results and flow visualization of the wingsuit, by analyzing the spanwise and chordwise vortex created through the surface and edge of the wing and studying the vortex created through the backpack on the Force and moment coefficients. The lift and drag forces increase simultaneously with an increase in the angle of attack from 0° to 40°. Towards AOA=10°, lift-to-drag shows an increase in the trend, then a decline. It can be assumed that AOA=10° was optimal for this wingsuit model in terms of lift-to-drag ratio. This result must be confirmed by other wingsuit models. Flow separations can also be observed in flow structure when a stall occurs at high angles of attack (a notable drop in lift force value indicates a detached flow). Compared with another study of results, lift force for this specific wingsuit significantly drops when AOA=35° (Ansari et al., 2018).

Figure 8(a) demonstrates the wingsuit's superior maneuverability due to the gentle slope in the post-stall area. Additionally, the experimental drag coefficient curve does not oscillate over the angles of attack. Lift-to-Drag

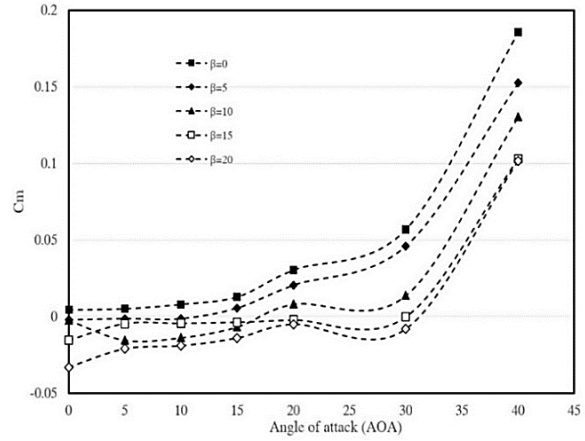

(a) Pitching moment coefficient

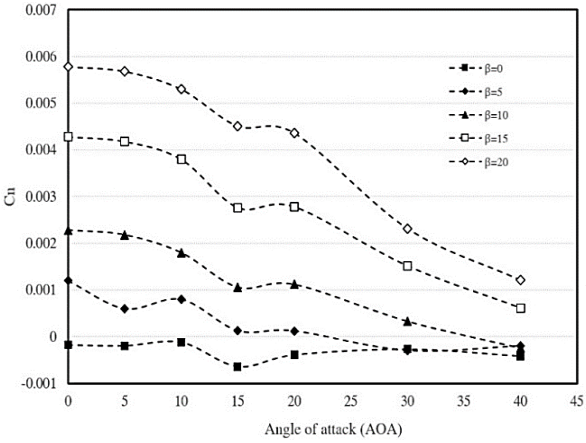

b) Yawing moment coefficient

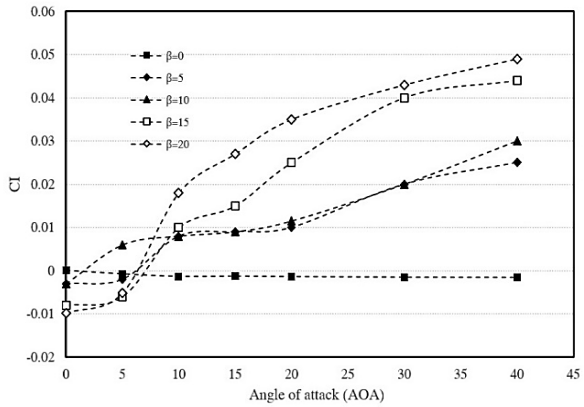

(c) Rolling moment coefficient

Fig. 9 Analysis of Pitching, Yawing and Rolling moment coefficients for different AOAs and β at Re≈1.3×10⁶

ratio increases as the angle of attack increases from 0° to 10°. Increasing lift-to-drag ratios reach AOA=10° and begin to decrease afterward (Fig. 8(d)).

A wingsuit's lateral directional characteristics will be determined by the relative strength of its directional stability and dihedral effects (Clarke & Gutman, 2017). In contrast to conventional flight, the model's shape contributes to strong directional stability. However, when the wingsuit begins to yaw, the model posture also produces a larger rolling moment, which creates a cross-coupling issue. wingsuit flight conditions caused the roll and yaw movements to be slightly reduced due to the damping effect that results from the informal posture's low directional stability. A change in dihedral angle, as determined by aerodynamic principles, can alter the angle of attack on a wing in sideslip mode by altering the lift distribution along the spanwise wing section. This changes the lateral directional aerodynamic derivatives of the wing.

As a result of comparison and validation of experimental studies, Figs (8,9) shows the number of parameters related to lateral stability calculated for low sideslip angles (0◦ to 20◦).

3. COMPUTATIONAL FLUID DYNAMICS STUDY

3.1 Numerical Setup

In the first stage, modeling software was used to develop the geometry. Each boundary has a named selection before meshing. The front face was assigned the inlet, while the back face was assigned the outlet. The model was symmetric, so only half of it was simulated. This plane was assigned to be the symmetry boundary, so all aspects of the domain were mirrored afterward. A wall boundary was assigned to the wing s surfaces along with the other remaining domain faces. Based on wingsuit length (L_m = 0.7 m) and the recommendations outlined in Fig. (10) sufficiently large size is required so that the far-field properties do not adversely affect the near-wall flow, the domain size was calculated to be 8.4 m × 4.5 m × 2.8 m. The mesh structure with perhaps the lowest number of elements was determined through a grid study. Meshes should be able to gather flow characteristics on a personal computer and also be made to fit the flow characteristics. Starting from coarse elements (0.5 Mio. elements), several mesh structures were examined. After a few iterations, a second-order high-resolution scheme was applied to better resemble the fluid flow characteristics. Boundary initializations were set from the inlet, and the second-order simulations were run for 7500 iterations. Thereafter, the lift and drag forces of each generated grid were calculated. The main parameters that were changed were the surface area on the wingsuit body, the number of inflation layers, and the element size in the main flow (far-field). A boundary layer resolved at the wall refined the grid close to the wall. The SST kω model is used at the near-wall grids with 10 inflation layers and a growth ratio of 1.2 in order to resolve the viscous sub layer (Subramanya, 2022).

3.2 Mesh Independence and Grid Quality

In order to determine the grid resolution, a suitable value for the wall y+ was taken into account. Using the log-law, we can determine the maximum and minimum distance between near-wall cells and walls assuming equilibrium boundary layers and fully developed flows. Distances are usually measured in dimensionless wall units, y+. A cell's centroid should be within the log-law layer if it is a wall-adjacent cell.

Based on Fig. (11) y+ calculated on the wingsuit (y+<1), the viscous sublayer thickness was determined. To capture the boundary layer's characteristics, a high resolution is required. We also discretized the outer flow

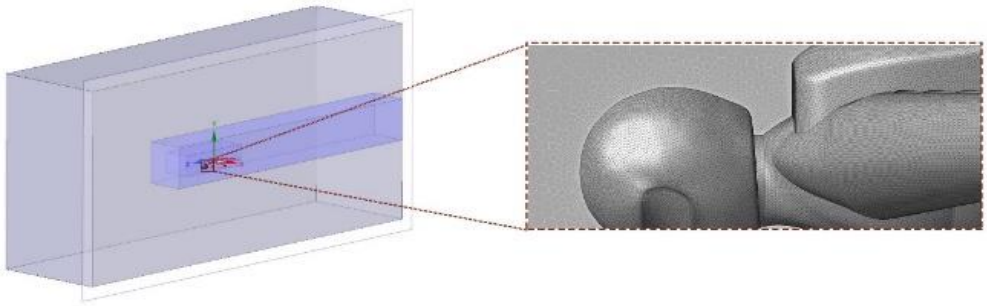

(a) (b)

Fig. 10 Schematics of domain with boundary conditions (a) Wingsuit mesh(b)

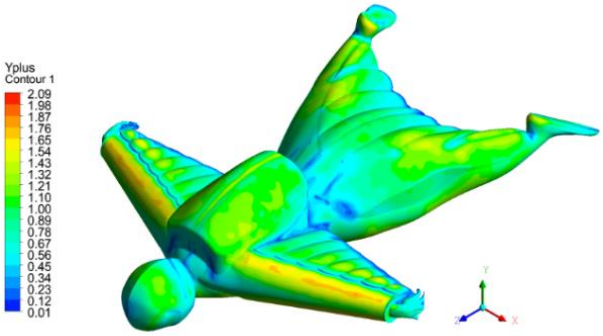

Fig. 11 Contour of y+ on wingsuit model

using polygons. A mesh of three million polygons ultimately produced the best results. As the number of polygons increased above 3M nothing much changed. Thus, the 3M mesh was chosen.

In a special case of simulating the Wingsuit model, the Grid Convergence Index (GCI) was used to determine whether the solution converged independently (Rumsey, 2016). Model length is 0.7 m, and Reynolds number is 1.5×10^6 for this study. Table 2 shows the specifications of each grid as well as the results of the simulation. In the analysis of independence from the mesh, 1% is considered an acceptable percentage difference between the answer of the smallest grid and item 3. Thus, grid meshing number 3 has been used as the basis for mesh production in simulations due to its acceptable accuracy and cost and time savings.

3.3 CFD Simulation Results

Results from the simulation of the wingsuit model are given in Figs. (12, 14). These values are presented graphically and commented on this section.

Bubbles begin to form at AOA=15°. The stall region begins at AOA=30°. The separation bubble grows as the angle of attack increases, and eventually a relatively large recirculating separation bubble forms on the top surface of the optimized at AOA=30°, covering the entire wing.

In the recirculating separation zone of the wingsuit model, values of shear stress can explain the high Drag coefficient. It is evident to see separation strips at the top of the wing at AOA=30°, there is deflection and wingtip vortices.

Table 2 Mesh independence study

Grid	S_{ref} [m^2]	Number of Cells	Lift Coefficient	Deviation (%)
1	0.22	537327	0.125	-
2	0.22	1323025	0.145	**2%**
3	0.22	3109211	0.156	**1.1%**
4	0.22	4214581	0.158	**0.2%**

Although a separation bubble forms for the angle of attack higher than AOA=30°, the wavy wing maintains a relatively high lift coefficient in the post-stall region. (Fig. (12)). A lot of numerical simulation hasn't been done with wingsuit profiles. Using Finite Volume method on a structured grid, the Reynolds Averaged-Navier-Stokes equations were solved using CFD. The Reynolds number reported in their study was 10^6 and the turbulence model used was kω (Omholt, 2011). The present study was accompanied by a numerical analysis.

A wingsuit model has been developed to simulate a pre-stall incidence at AOA=35° in $Re=10^6$ for an incompressible flow around the WMN7 wavy shape. The wavy HW wing surface (WMN7) was validated using experimental data in flow visualization and aerodynamics force and moment.

This study, all qualitative and quantitative results will be discussed. The results validated in this work are surface flow, velocity distribution, and pressure coefficient distribution. Typically, only a few results are evaluated for wingsuit cross-section, but all results are described for wingsuit, which is of greater interest. Because the leading edge is rounded, the position of the vortex breakdown is not fixed. Wingsuit drag and lift coefficients are also calculated. The streamlines of velocity around a wingsuit for HW and LW wings for various angles of attack can be seen in Fig. (12), and the produced spanwise vortex is stronger and positioned on the rear of the backpack. In the chord length region, a chordwise vortex forms, and its attachment and separation lines are close in proximity to the TE of the wing. Furthermore, the presence of primary and secondary LE (outer) counter-rotating vortices can be detected. Most of the test conditions are accompanied by the onset of the primary vortex, especially for the HW wing. By looking at streamlines, secondary vortices were not detected. In the streamlined pictures, you can see where the primary and secondary vortexes are separated and attached. The streamlines to vortex breakdown around

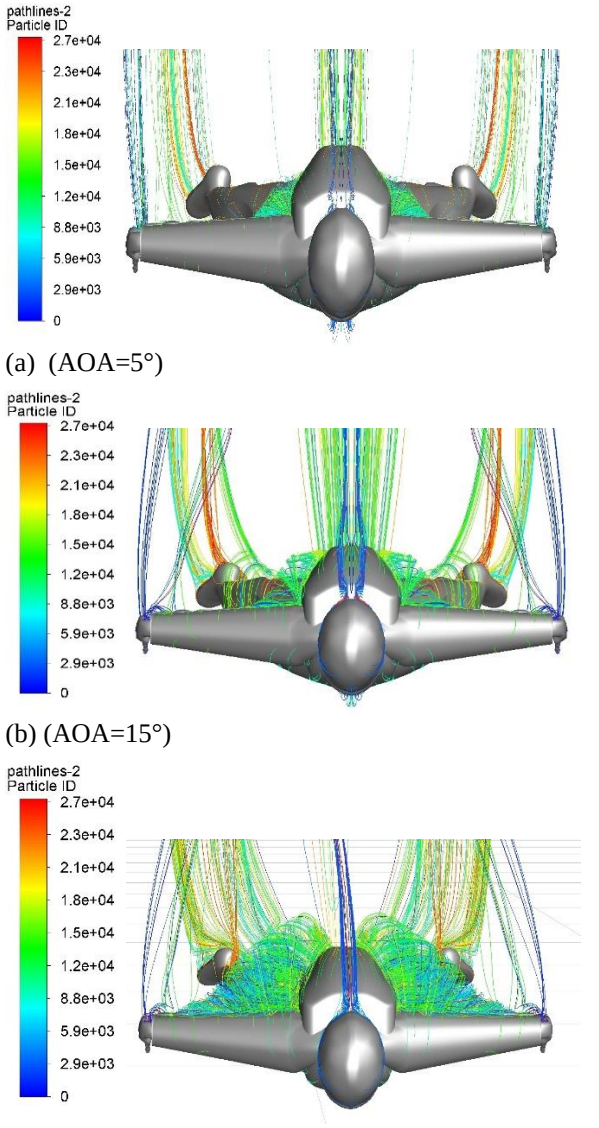

(a) (AOA=5°)

(b) (AOA=15°)

(c) (AOA=30°)

Fig. 12 3D velocity streamlines and wake vortices at different angles of attack at Re ≈ 1.5×10^6 (a,b,c) 3D velocity streamlines

the rear edges of the legs are shown in Fig. (12). Both LE and all angles of attack were able to see the development of the primary vortex. Vortex generation usually occurs earlier on HW geometry.

3D wake vortices derived from the 3D cross-section depict the same trends as the velocity streamlines in (Fig. 12). 3D Streamwise vortex generated by wingtip vortices shows an increase in turbulence with an increase in the angle of attack. By reducing the aspect ratio of the wing, the tip vortices produce crossflow that reaches a larger Area of the wing, resulting in nonlinear drag increases at higher angles of attack. The axial velocity and Pressure Coefficient distribution are plotted for different cross sections at z=0 m and z= ± 0.1 m from the main coordinate zero point in Z-direction (Fig. 13)

Differential pressure on the upper and lower of the wing causes the wingtip vortices to separate (Fig. 14). When the angle of attack is increased from 5° to 30°, it appears that the flow detaches from the surface upstream

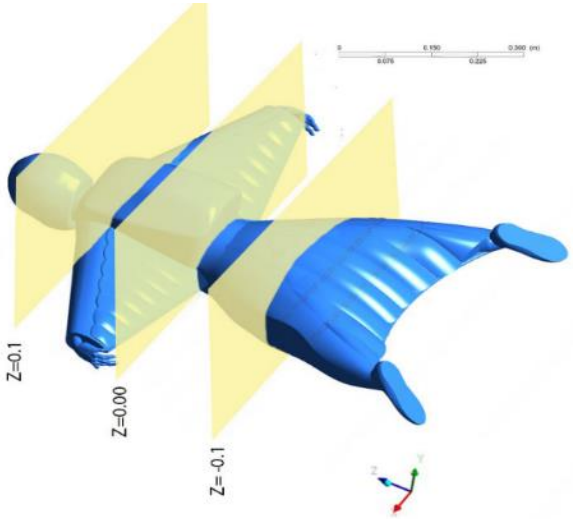

Fig. 13 Cross section planes to visualize the desired parameters (Flat posture, at AOA=15°)

of the wing and induced drag and total drag increase when the wingtip vortices detach.

In the axial velocity distribution section of Fig. (14), we plot the axial velocity distribution for different cross-sections on the main coordinate at AOA=15° disrupts the flow pattern in this posture, causing the flow structure to appear circular for the peak and trough of ridges on the wing. A pressure-related parameter, C_P, was also explored in order to understand the flow structure around of model. Circular vortices are visible at the wingtips (z = 0). The vortices are shown at z=0 and z=0.1 m for each section of the HW wing, making analysis of the flow structure more difficult.

4. COMPARISON OF CFD SIMULATION AND WIND TUNNEL STUDY

First, the CFD numerical procedure is varied. After discussing the wind tunnel study in general, the numerical simulation and the wingsuit model are validated based on the wind tunnel study and the real wingsuit. Lastly, the aerodynamic differences between the two methods are discussed.

Based on previous experiments done on a wingsuit, Effective angles of attack were chosen for the wind tunnel experiment on the wingsuit. As the highest glide ratio, the most important wingsuit performance characteristic was expected to lie between AOA = 30° and AOA= 40°, no angles above AOA = 40° were tested.

The lift and drag both increases with increasing angle of attack up to 35°, then the lift decreases while the lift-to-drag ratio (L/D) continues to rise until AOA = 10°. An aspect ratio variation 2.22 is observed at the best glide ratio (3.5). In steady flight, wings suits have a low glide ratio of around 2.5 compared to other glider types because of their low aspect ratio (Alaei & Valipour, 2023).

The lift and drag coefficients are calculated using Numerical simulation. with consider a surface area in the Aerodynamics coefficient of 0.22 m^2.

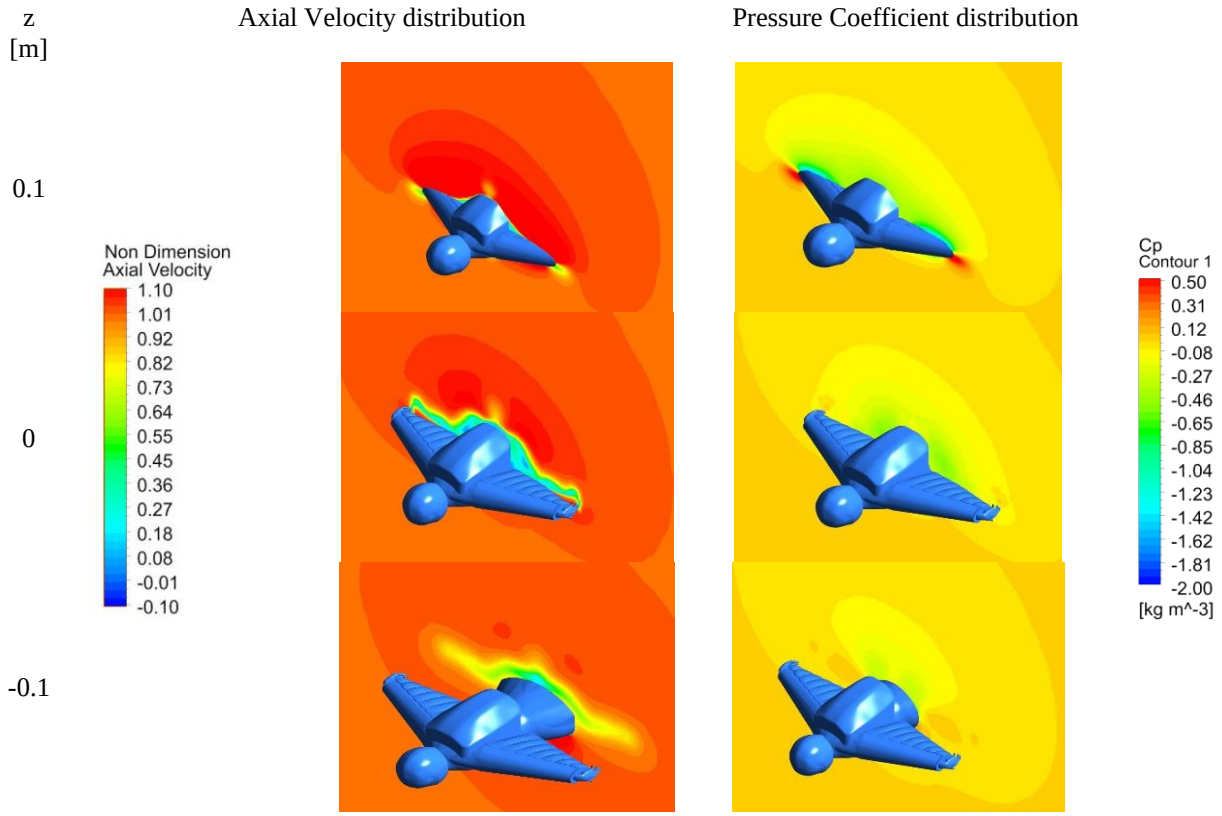

Fig. 14 An axial velocity distribution is shown on the left below, followed by a pressure coefficient distribution on the wingsuit flyer at a AOA=15° and with a cross-section of z=0 and z=±0.1 m perpendicular to the wingsuit flyer

The lack of data for higher angles of attack is a major drawback since it restrains a full comparison to the simulation predictions. Trends can however still be evaluated. Generally speaking, the curves of the simulation and experimental data are similar. In other words, the qualitative aerodynamic characteristics of a wingsuit are captured by the numerical method used in this study (Fig. 15).

Based on the results obtained from the examined wingsuits model, some were selected which enable comparisons between the wingsuit flight condition and the mentioned experimental parameters.

- Performance/handling - Furthermore, by changing the flight angle of attack from AOA=0° to AOA=10°, an increase in glide ratio was expected. One-piece wingsuits generally achieve a higher glide ratio than two-piece wingsuits; because of the larger wing surfaces.
- The angle of attack - The three flight angles 15°, 20°, and 25° do not necessarily result in a steady increase in glide ratio. Taking into account a flow separation at the object from AOA=30°, a suitable angular range will be identified, in which maximum values can be achieved.

Wind tunnel experiments provide reference data for the forces of interest to enable validation of the numerical results. Despite considerable efforts and costs involved in these experiments, these are currently an essential part of the development process of wingsuits. However, the aim is to be able to predict the results of different wingsuit variants and postures

Without such expensive experimental tests. To achieve this, the wind tunnel results are very helpful in validating the simulation results.

5. RESPONSE SURFACE METHODOLOGY (RSM)

Response surface methodology can be utilized when modeling continuous factors on curved quadratic surfaces. A response surface can be used to locate the minimum or maximum response if any exists within the factor area. (Kim et al., 2022). Curved surfaces cannot be fitted by standard two-level designs, since each factor must have three distinct values. Compared to central composites, the BBD is an alternative to two-level fractional factorials. For axial points, all but one factor is zero, which sets the outer value at the outer value. BBD (Box-Behnken design) features only three levels for each factor. One important difference between the two types of designs is that BBD does not include points at the cube's vertices. A factor's range determines its range. Due to engineering considerations, sometimes avoiding these points is desirable. Due to engineering considerations, sometimes avoiding these points is desirable (Chaisson et al., 2022). As a result, predictions near the vertices are highly uncertain compared to the central composite design. When there is a measurable, continuous, and controllable process factor, and a negligible error, it is referred to as an RSM procedure, as follows:

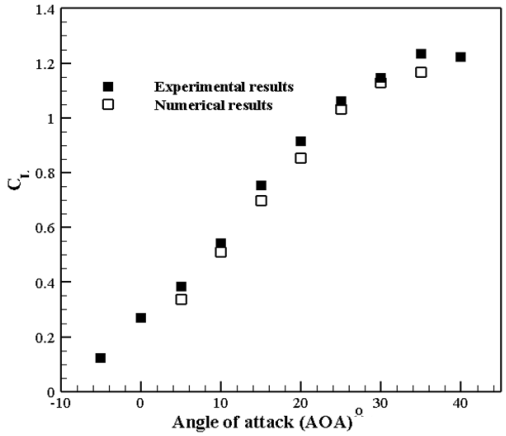

(a) Lift coefficient

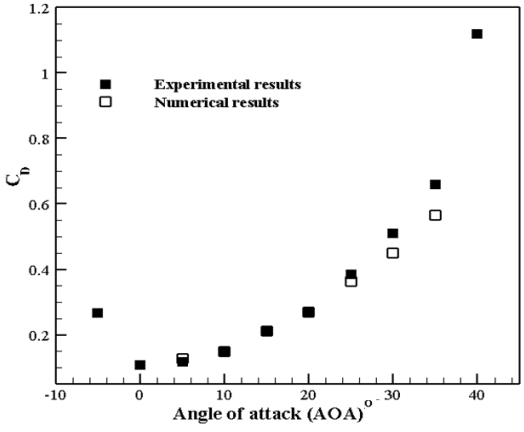

(b) Drag coefficient

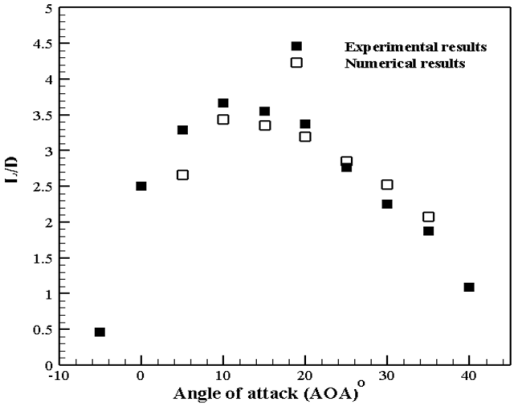

(c) L/D

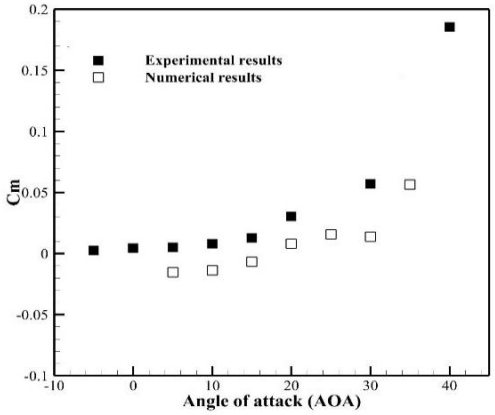

(d) Pitching moment coefficient

Fig. 15 Lift, Drag, pitching moment coefficients and Performance for angle of attack- comparing literature results (experiment - black square), (simulation results SST model - white square)

Table 3 Design parameters for Box-Behnken Design (BBD) and Response Surface Methodology (RSM)

Factors	Dimension	Symbolic sign	Low level (-1)	Middle level (0)	High level (+1)
V	m/s	A	30	35	40
β	Degree	B	0	5	10
AOA	Degree	C	0	15	30

- The response of interest is measured adequately and reliably through a series of experiments.
- The best-fit second-order response surface is developed using a mathematical model.
- Experimental parameters are selected to produce the optimum response value.
- Process parameters are shown in two-dimensional and three-dimensional plots.

In this case, experiments are designed to measure the response in a reliable and adequate manner (Jun et al., 2006). To fit the second-order model used in this study, BBD is a very efficient design tool. A polynomial equation was used to fit the experimental data with the RSM. The minimum CD value was determined by a three-level, three-factor BBD method based on the values of the extraction variables (Eq. (2)).

The independent variables are velocity (A), side angle (B), and AOA (C) in the model (WMN7). The responses are coefficient of drag and aerodynamic efficiency. As can be seen from Table 3, the response surface analysis contains the response values and the BBD matrix. The response surface was analyzed using a second-order polynomial model.

$$RC = \alpha_0+\alpha_1 A+\alpha_2 B+\alpha_3 C+\alpha_{12} AB+\alpha_{13} AC+\alpha_{23} BC+\alpha_{11} A^2+\alpha_{22} B^2+\alpha_{33} C^2 \quad (2)$$

Level of the investigated design parameters ranging from the low to the middle and the high, is presented in Table 3. In addition, the CD_{min} and Lift-to-drag ratio (L/D) values are presented in Table 4.

5.1 Analysis of Variance (ANOVA)

Analyzing variance is a method of determining whether the parameters under investigation differ from the norm (Ali et al., 2018). The probability of dimension flaws, uncontrolled parameters, and sum of squares are determined using F statistics and the sum of squares.

Table 4 BBD-based design of experiments (DoE) Matrix

Factor 1	**Factor 2**	**Factor 3**	**Response 1**	**Response 2**	**Response 3**	**Response 4**	**Response 5**	**Response 6**	**Response 7**
A: Velocity (V)	B: side angle (β)	C: Angle of Attack (AOAO)	CD	CL	CY	Cm	CI	Cn	L/D
30	0	15	0.212333	0.714386	0.009	0.0234	-0.0013	-0.000821	3.36446
40	10	15	0.282979	0.605957	0.0452567	-0.0273945	0.0118078	0.0040664	2.14135
35	5	15	0.285896	0.635787	0.0319023	-0.0299877	0.0091234	0.0032313	2.55751
30	10	15	0.294213	0.73142	0.215	-0.05	-0.002115	0.001	2.14613
35	10	30	0.556044	1.02359	0.126102	0.111101	0.0301432	0.0012313	1.84084
30	5	0	0.153026	0.221554	0.00369	-0.011416	-0.003	0.0013	1.25177
35	5	15	0.275896	0.665787	0.0401023	-0.0259877	0.0088534	0.0030313	2.35751
35	5	15	0.273896	0.659787	0.0382023	-0.0219877	0.0119234	0.0036313	2.65751
40	0	15	0.209213	0.66782	0.0091231	0.0244345	-0.0011766	0.0001444	3.19206
40	5	30	0.480294	1.07629	0.0872456	0.162017	0.0230288	0.0078649	2.24091
35	5	15	0.272996	0.615787	0.0305102	-0.0209877	0.0098234	0.0031513	2.41751
35	0	30	0.38421	1.03862	0.0162232	0.201035	-0.0014204	0.003234	2.70326
40	5	0	0.147792	0.186091	0.0039356	-0.0069399	0.0032879	0.0048164	1.25914
35	5	15	0.276896	0.649787	0.0391023	-0.0289877	0.0107234	0.0039313	2.8751
35	10	0	0.159343	0.202599	0.0045423	-0.0146908	0.0061432	0.0060313	1.27147
30	5	30	0.485528	1.08176	0.087	0.0048	0.02	0.0072	2.228
35	0	0	0.121709	0.182786	-0.0001857	0.0015476	2.34E-05	0.000634	1.50182

The results for the response surface models presented in Table 4 were obtained using Design Expert software through analysis of variance (ANOVA). The regression model was found to be statistically significant by ANOVA according to Table 5(a), since its F-value (412,33) was extremely high, but its p-value was extremely low ($p<0.0001$). For the lack of fit, the F-value (4.63), which was insignificant, confirmed the validity of the model. In addition, the low coefficient of variation (CV) of 2.87 clearly indicated that the experimental results were precise and reliable. Observed values and predicted values have a high correlation, as indicated by high R^2-sq, R^2-sq (adj), and p-value parameters. This response was significantly related to the quadratic model, as determined by ANOVA

Table 5 ANOVA for aerodynamics and moment coefficient

a) Drag coefficient (C_D)

Source	Sum of Squares	DOF	Mean Square	F-value	p-value	
Model	0.2514	9	0.0279	412.33	< 0.0001	significant
A-A	0.0001	1	0.0001	1.14	0.3217	
B-B	0.0167	1	0.0167	246.01	< 0.0001	
C-C	0.2192	1	0.2192	3235.93	< 0.0001	
AB	0.0000	1	0.0000	0.2430	0.6372	
AC	0.0000	1	0.0000	0.0000	1.0000	
BC	0.0045	1	0.0045	66.47	< 0.0001	
A^2	0.0003	1	0.0003	4.03	0.0848	
B^2	0.0016	1	0.0016	23.35	0.0019	
C^2	0.0095	1	0.0095	140.80	< 0.0001	
Residual	0.0005	7	0.0001			
Lack of Fit	0.0004	3	0.0001	4.63	0.0864	not significant
Pure Error	0.0001	4	0.0000			
Cor Total	0.2518	16				
R^2 = 0.9981				Std. Dev.	0.0082	
Adjusted R^2 = 0.9957				Mean	0.2866	
Predicted R^2 0.9760				C.V. %	2.87	
Adeq Precision 66.9061						

b) Side force coefficient (C_Y)

Source	Sum of Squares	df	Mean Square	F-value	p-value	
Model	0.0194	9	0.0022	37.13	< 0.0001	significant
A-A	9.485E-08	1	9.485E-08	0.0016	0.9689	
B-B	0.0044	1	0.0044	75.09	< 0.0001	
C-C	0.0116	1	0.0116	199.78	< 0.0001	
AB	4.452E-09	1	4.452E-09	0.0001	0.9933	
AC	0.0000	1	0.0000	0.0000	1.0000	
BC	0.0028	1	0.0028	47.62	0.0002	
A^2	5.400E-09	1	5.400E-09	0.0001	0.9926	
B^2	0.0003	1	0.0003	5.66	0.0490	
C^2	0.0004	1	0.0004	6.60	0.0370	
Residual	0.0004	7	0.0001			
Lack of Fit	0.0003	3	0.0001	5.59	0.0649	not significant
Pure Error	0.0001	4	0.0000			
Cor Total	0.0198	16				
R^2 = 97.95%				Std. Dev. = 0.0076		
Adjusted R^2 = 95.31%				Mean = 0.0363		
Predicted R^2 = 72.87%				C.V. %=21.00		
Adeq Precision = 22.0285						

c) Pitching moment coefficient (C_m)

Source	Sum of Squares	df	Mean Square	F-value	p-value	
Model	0.1009	9	0.0112	446.36	< 0.0001	significant
A-A	0.0001	1	0.0001	4.52	0.0711	
B-B	0.0067	1	0.0067	266.47	< 0.0001	
C-C	0.0554	1	0.0554	2205.01	< 0.0001	
AB	0.0001	1	0.0001	4.63	0.0684	
AC	1.512E-06	1	1.512E-06	0.0602	0.8132	
BC	0.0014	1	0.0014	54.05	0.0002	
A^2	0.0004	1	0.0004	15.71	0.0054	
B^2	0.0003	1	0.0003	12.15	0.0102	
C^2	0.0355	1	0.0355	1413.26	< 0.0001	
Residual	0.0002	7	0.0000			
Lack of Fit	0.0001	3	0.0000	2.26	0.2233	not significant
Pure Error	0.0001	4	0.0000			
Cor Total	0.1011	16				
R2 = 99.83%				Std. Dev. = 0.0050		
Adjusted R^2 = 99.60%				Mean = 0.0262		
Predicted R^2 = 98.15%				C.V. % = 19.14		
Adeq Precision = 65.2405						

d) Lift coefficient (C_L)

Source	Sum of Squares	df	Mean Square	F-value	p-value	
Model	1.50	3	0.4991	599.53	< 0.0001	significant
A-A	0.0009	1	0.0009	1.03	0.3279	
B-B	0.0025	1	0.0025	2.94	0.1099	
C-C	1.49	1	1.49	1794.61	< 0.0001	
Residual	0.0108	13	0.0008			
Lack of Fit	0.0092	9	0.0010	2.54	0.1915	not significant
Pure Error	0.0016	4	0.0004			
Cor Total	1.51	16				
R^2 0.9928				Std. Dev.	0.0289	
Adjusted R^2 0.9912				Mean	0.6370	
Predicted R^2 0.9862				C.V. %	4.53	
Adeq Precision 64.2556						

e) Yawing coefficient (C_n)

Source	Sum of Squares	df	Mean Square	F-value	p-value	
Model	0.0059	9	0.0007	20.84	0.0003	significant
A-A	6.209E-07	1	6.209E-07	0.0196	0.8926	
B-B	0.0027	1	0.0027	84.98	< 0.0001	
C-C	0.0020	1	0.0020	62.63	< 0.0001	
AB	4.642E-08	1	4.642E-08	0.0015	0.9705	
AC	0.0000	1	0.0000	0.0000	1.0000	
BC	0.0006	1	0.0006	20.20	0.0028	
A^2	0.0000	1	0.0000	0.6923	0.4329	
B^2	0.0005	1	0.0005	15.62	0.0055	
C^2	0.0001	1	0.0001	2.11	0.1893	
Residual	0.0002	7	0.0000			
Lack of Fit	0.0002	3	0.0001	3.93	0.1096	not significant
Pure Error	0.0001	4	0.0000			
Cor Total	0.0062	16				
R2 = 96.40%				Std. Dev. = 0.0056		
Adjusted R^2 = 91.77%				Mean = 0.0259		
Predicted R^2 = 55.58%				C.V. % = 21.73		
Adeq Precision = 15.7955						

f) Lift-to-drag ratio (L/D)

Source	Sum of Squares	df	Mean Square	F-value	p-value	
Model	6.36	9	0.7063	14.07	0.0011	significant
A-A	0.0031	1	0.0031	0.0613	0.8116	
B-B	1.41	1	1.41	28.14	0.0011	
C-C	1.74	1	1.74	34.62	0.0006	
AB	0.0070	1	0.0070	0.1399	0.7195	
AC	7.672E-06	1	7.672E-06	0.0002	0.9905	
BC	0.0999	1	0.0999	1.99	0.2013	
A^2	0.0030	1	0.0030	0.0602	0.8132	
B^2	0.0520	1	0.0520	1.04	0.3425	
C^2	3.08	1	3.08	61.28	0.0001	
Residual	0.3515	7	0.0502			
Lack of Fit	0.1822	3	0.0607	1.44	0.3571	not significant
Pure Error	0.1693	4	0.0423			
Cor Total	6.71	16				
R^2= 94.76%				Std. Dev. = 0.2241		
Adjusted R^2 = 88.03%				Mean = 2.24		
Predicted R^2 = 0.5260				C.V. % = 10.02		
Adeq Precision = 12.1713						

(Table 5). Furthermore, there were very high values for the R^2-sq [adj] and sq-R^2 for the response level models (99.57% and 99.81%, respectively) indicating high regression coefficients in the predicted C_D response models.

At the 98.99% probability level, C (angle of attack) and B (side angle) parameters had no significant effect. BC interaction had a significant level and influenced our response. C_D response was also best influenced by the interaction between the second and third parameters, and

the third parameter increased C_D more than the second parameter. The side force coefficient and pitching moment coefficient are calculated similarly to the drag coefficient in Table 5(b,c).

5.2 Modeling Regression and Diagnostic Tests

An experimental design and results for the Box-Behnken experiment are presented in Table 4. As a result of the results, C_D and (L/D) extraction yields are strongly dependent on the extraction conditions.

Based on the experimental data, multiple regression analysis could be used to predict the C_{Dmin} and $(L/D)_{max}$ (Eq. (3)) and obtain the values shown in Table 6 (a,f).

$$C_{D\,min}=0.2771-0.0031(V)+0.0456(AOA)+0.1655(\beta)-0.0020(V)(AOA)+0.0336(AOA)(\beta)-0.0080(V)^2-0.0194(AOA)^2+0.0476(\beta)^2 \quad (3)$$

$$(L/D)_{max} = +2.57-0.0196A-0.4202B+0.4661C+0.0419AB+0.0014AC-0.1580BC+0.0268A^2+0.1112B^2-0.8549C^2$$

To determine the accuracy of the obtained correlation, residual plots of C_{Dmin} are plotted in Fig. 16(a). A scatterplot reveals a generally linear pattern, which indicates a normal distribution of errors. A comparison of Eq. (3) predictions against actual values is shown in Fig. 16(b), showing a perfect fit and, thus, model accuracy. As scatters approach or fall on a 45-degree line, errors decrease. residuals and run numbers for C_{Dmin} are shown in Figs. 16(c) and 16(d), respectively. The present quadratic model can only explain 0.43% of variations, which indicates a good mathematical relationship between factors and responses. R^2 and adj-R^2 are, respectively, 99.57% and 99.81%.

Predicted values are highly correlated with observed values by high R2-sq, R2-sq(adj) and P-Value parameters for L/D. This answer was significantly influenced by the quadratic model based on the ANOVA table results. Furthermore, high R2-sq values (88.03% and 94.76%) A high regression coefficient and highly significant regression coefficients were found in the predicted models for L/D response. Our response was effective with a high probability of 99% for the parameters x2 (side angle) and x3 (angle of attack), but the disproportion had no significant effect. Effectiveness was achieved. A positive effect was observed on Lift-to-drag ratio response when

Table 6 Regression Coefficients

a) Drag coefficient (C_D)

Regression terms	Coefficients regression model	P value
intercept	+0.2771	< 0.0001
A	-0.0031	0.3217
B	+0.0456	< 0.0001
C	+0.1655	< 0.0001
AB	-0.0020	0.6372
BC	+0.0336	1.0000
A^2	-0.0080	< 0.0001
B^2	-0.0194	0.0848
C^2	+0.0476	0.0019

b) Side force coefficient (C_Y)

Regression terms	Coefficients regression model	P value
intercept	+0.0360	< 0.0001
A	+0.0001	0.9689
B	+0.0233	< 0.0001
C	+0.0381	< 0.0001
AB	+0.0000	0.9933
AC	+0.0000	1.0000
BC	+0.0263	0.0002
A2	-0.0000	0.9926
B2	-0.0088	0.0490
C2	+0.0095	0.0370

c) Pitching moment coefficient (Cm)

Regression terms	Coefficients regression model	P value
intercept	-0.0256	< 0.0001
A	0.0038	0.0711
B	– 0.0289	< 0.0001
C	0.0832	< 0.0001
AB	0.0054	0.0684
BC	0.0006	0.8132
A2	- 0.0184	0.0002
B2	0.0058	0.0054
C2	0.0918	0.0102

d) Lift coefficient (C_L)

Regression terms	Coefficients regression model	P value
intercept	0.6370	< 0.0001
A	-0.0104	0.3279
B	-0.0175B	0.1099
C	0.4322C	< 0.0001

e) Yawing coefficient (C_n)

Regression terms	Coefficients regression model	P value
intercept	+0.0340	0.0003
A	0.0003	0.8926
B	0.0183	< 0.0001
C	-0.0158	< 0.0001
AB	0.0001	0.9705
BC	-0.0126	0.0028
A2	0.0126	0.4329
B2	0.0108	0.0055
C2	0.0040	0.1893

f) Lift-to-drag ratio (L/D)

Regression terms	Coefficients regression model	P value
intercept	**+2.57**	0.0011
A	**-0.0196**	0.8116
B	**-0.4202**	0.0011
C	**0.4661**	0.0006
AB	**0.0419**	0.7195
AC	**0.0014**	0.9905
BC	**-0.1580**	0.2013
A2	**0.0268**	0.8132
B2	**0.1112**	0.3425
C2	**-0.8549**	0.0001

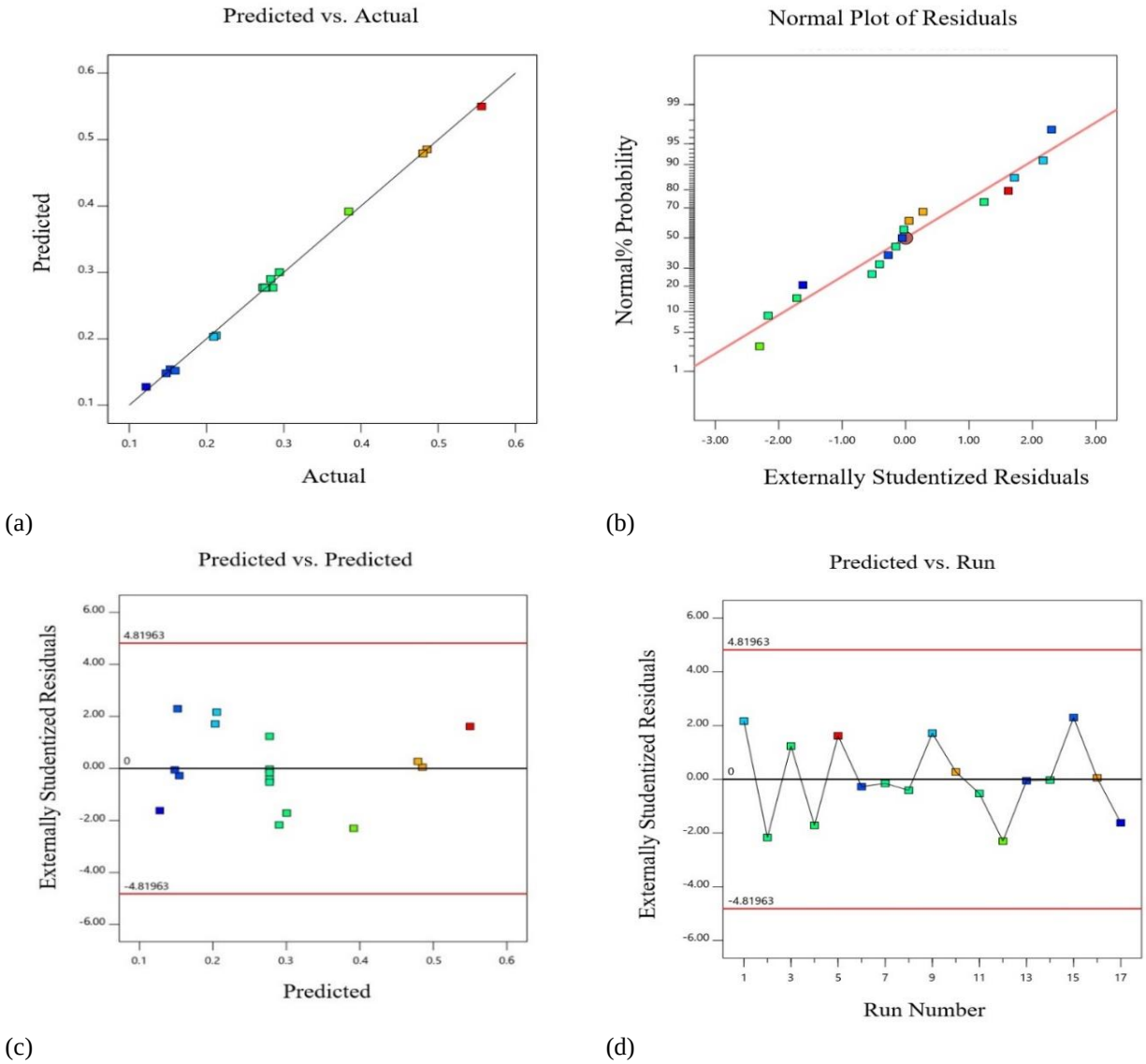

Fig. 16 Residual plots for C_{Dmin}: (a) Normal probability, (b) Perfection of fit, (c) residuals versus predicted, and (d) residuals versus resulted numbers

the third items was increased, while a negative effect was observed when the second parameter was increased (Fig. 17).

5.3 Response Surface Analysis

Contour plots and their three-dimensional surfaces for Eq. (3) are illustrated in Fig. 18. There are two- and three-dimensional plots that can be drawn based on different combinations of parameters, which can be used to display the trend of variations in response across the selected range of input parameters and to show the influence of parameters on each other. The interaction between AOA and β was investigated at the middle level of c (C=0) and plotted in Fig. 17(a). When AOA and side angle reach a maximum value, C_D reaches its maximum value at the highest value of both (C=0). As a result of this analysis, a minimal point is found between B=0 and +1 and C=0 and +1. AOA and side angle were investigated simultaneously on C_D. (Fig. 17(a)). At high values of AOA and side angle, CD will be at its highest.

It is shown in Fig 17 that the results are not symmetrical opposite a line crossing at β=5°. In other words, the best response in the blue area can be achieved with B values of 0 to 8 and C values of 0 to 10.

The side force coefficient and pitching moment coefficient are calculated similarly to the drag coefficient in Fig. 17(b,c).

The side force coefficient (C_Y) and pitching moment coefficient (C_m) are calculated similarly to the drag coefficient (C_D) in Table 5(b,c) and the Cm min ,C_Y min could be obtained via the second-order polynomial in Eq. (2) and the values obtained in Table 6(b,c).

5.4 Optimization

RSM was used to optimize the minimum drag coefficient yield for the wingsuit. The experiment was repeated three times under different conditions, resulting in a set of experiments. According to the results, maximum CD occurs at high angles of attack and side angles. The optimal conditions, where low angles of attack

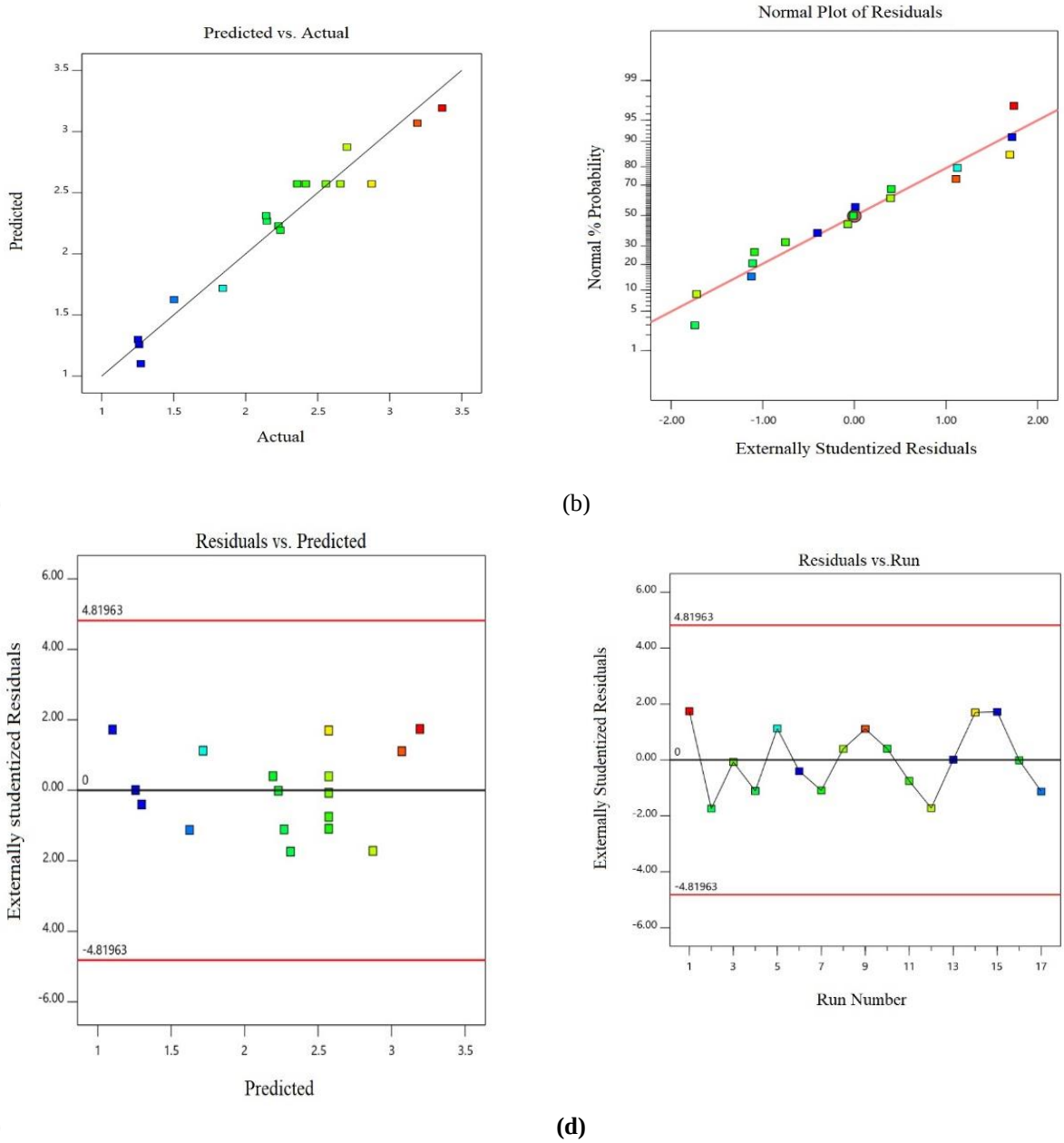

Fig. 17 Residual plots for $(L/D)_{max}$: (a) Normal probability, (b) Perfection of fit, (c) residuals versus predicted, and (d) residuals versus resulted numbers

occur, occur at V=30 m/s and AOA=0° with an accepted desire rate of 0.999. The optimal design parameters indicate that maximum performance is achieved when the side angle of the wingsuit is minimized.

6. CONCLUSION

A flying body's lift-to-drag ratio is one of the key parameters for determining aerodynamic efficiency. Force and moment determine the aerodynamic resulting effect on the body perpendicularly or parallel to the freestream velocity. We calculated lift and drag forces based on wind tunnel measurements for each wingsuit variation for comparison purposes. The hypothetical variation model was calculated only for the flat posture, because no real geometry on which the 3D CAD model was developed based, and it was developed mainly to evaluate how wing sizes can affect the flight behavior and the glide ratio.

According to the experiment results, the best flight performance (L/D) was measured at AOA=10, where the aim of this study was to determine whether the beginner wingsuit model has stability problems. The yawing momentum of the model increases strongly with the increase of the lateral angle, whereas it decreases with the increase of the angle of attack. The lift coefficient diagram shows that the model has the highest lift coefficient at AOA=35, but the L/D is greatly reduced due to the increased drag coefficient. With increasing angle of attack, pitch and roll moment coefficients increase greatly, whereas yawing moment coefficients decrease.

As the pitch moment coefficient analysis was run, different characteristics were observed in the asymmetric model deflecting roll characteristics. Since roll has a small moment of inertia, it can have a greater impact on angular acceleration than yaw and pitch, so asymmetric

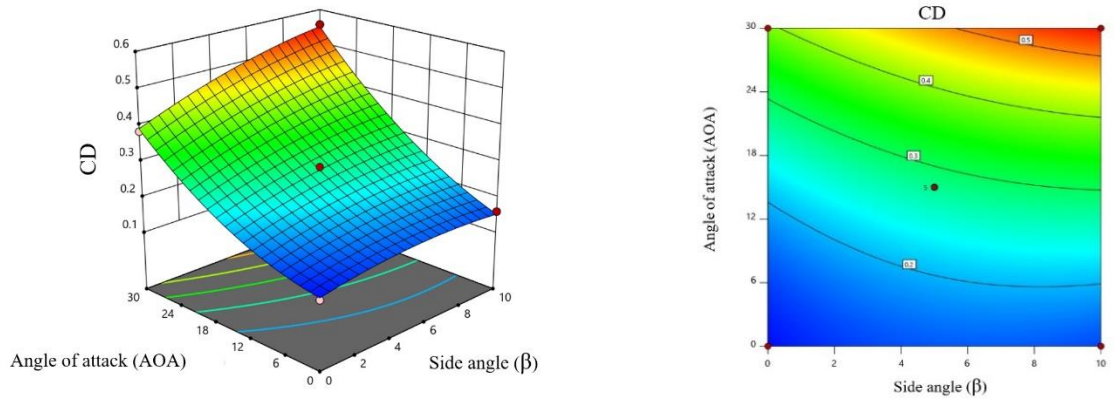

a) Drag coefficient (C_D)

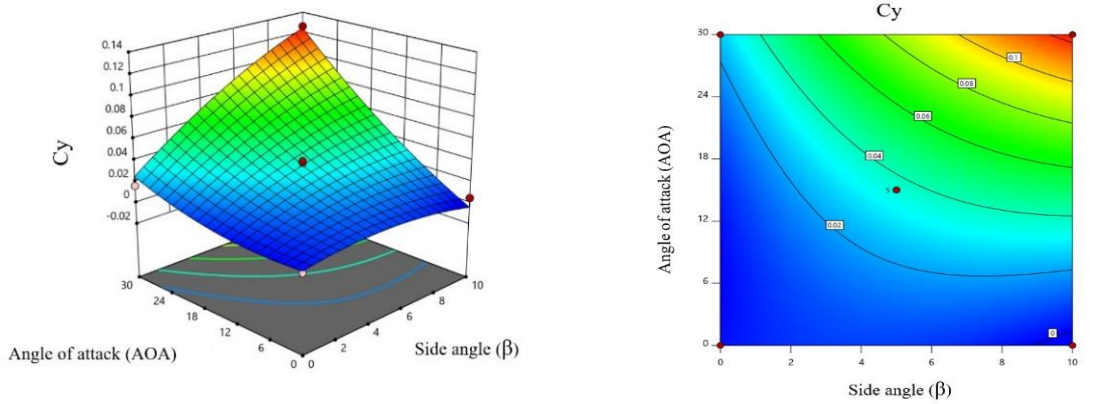

b) Side force coefficient (C_Y)

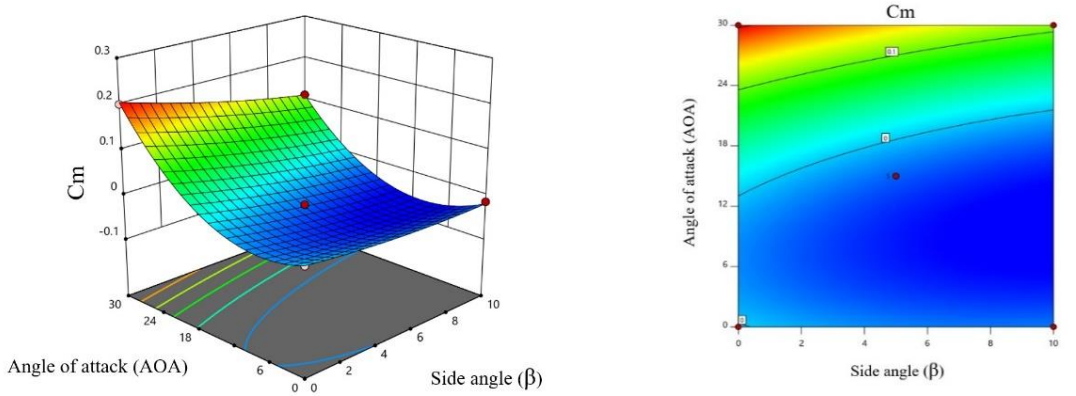

c) Pitching moment coefficient (Cm)

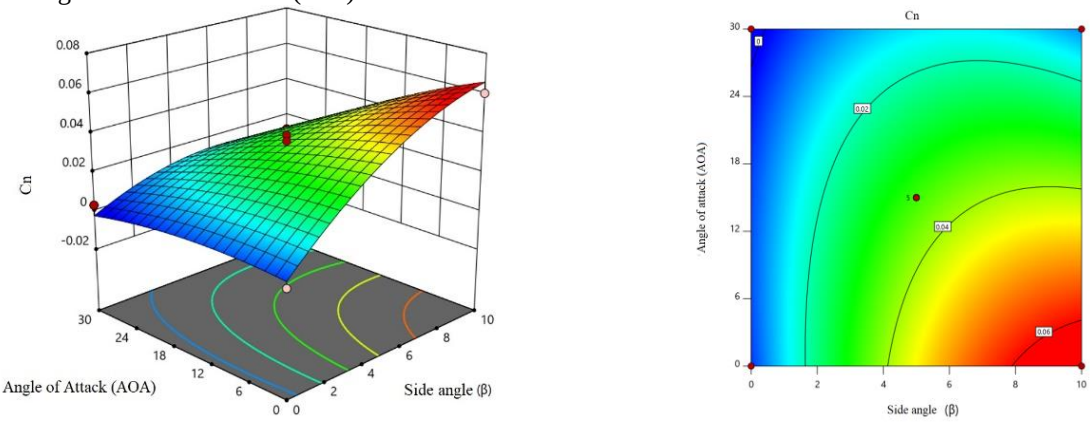

(c) Yawing moment coefficient (Cn)

Fig. 18 Contour and 3D response surface plots for the effect of angle of attack (AOA) and side angle (β) on aerodynamics and moment coefficient

movements can accelerate roll aggressively at high speeds. The results of this study suggest that if the wingsuit starts from a stable symmetrical position, it will remain stable. Further mechanics studies are needed to determine whether the pilot can handle the rotations in time.

Pilots who jump from planes or perform aerobatics may experience large rotational forces that could cause disorientation when their wingsuits initiate at an asymmetrical angle or position. Because the model has a great deal of stiffness, low pitch angles may be misleading when wingsuits have pitch angles greater than 10°. Camber decreases as wing segments angle toward the air stream.

It is difficult to determine whether the results from this study are accurate due to the uncertainty about the wingsuit shape. In order to validate the model, the shapes at specific angles could be acquired and compared with numerical simulations. The oscillating solution suggests that time-dependent phenomena in transient solvers should be further investigated.

Based on the results obtained from the examined wingsuits model, some were selected which enable comparisons between the wingsuit flight condition and the mentioned experimental parameters.

- The model configurations lead to lower pitching moment coefficient values at low angles of attack due to lower slopes of the curve at side angles. In addition, as a result of Tufts visualization, pitching moment values decrease much earlier as the stall approaches. With WMN7, the moment coefficient starts to increase rapidly at AOA=30° and, in most cases, the moment coefficient stays low throughout the entire attack angle range
- Aerodynamic performance of wingsuit models results in a minimum lift-to-drag value in most Reynolds number ranges due to the higher angle of attack at pre-stall due to the shape

ACKNOWLEDGEMENTS

The work was carried out with the support of the Department of Mechanical & Aerospace Engineering at K.N. Toosi University of technology. Thanks are due to Dr. Sohrab. Gholamhosein Pouryoussefy for his time, suggestions, and valuable conceptual contributions.

CONFLICT OF INTEREST

The authors declare that they have no known competing financial interests or personal relationships that could have appeared to influence the work reported in this paper.

FUNDING

No funds, grants, or other support was received.

COMPETING INTERESTS

Financial interests: The authors declare they have no financial interests.

AUTHORS CONTRIBUTION

All authors whose names appear on the submission made substantial contributions to the conception or design of the work and approved the version to be published.

REFRENCES

Abrams, M. (2007). *Birdmen, batmen, and skyflyers: Wingsuits and the pioneers who flew in them, fell in them, and perfected them*. Broadway Books.

Alaei, M. N., & Valipour, M. S. (2023). Experimental Alaei study of optimized beginner-level wingsuit. *Archive of Applied Mechanics*, 1-20. https://doi.org/10.1007/s00419-023-02381-9

Ali, B., Ouahiba, G., Hamid, O., & Ahmed, B. (2018). *Aerodynamic optimization of active flow control over S809 airfoil using synthetic jet*. 2018 International Conference on Wind Energy and Applications in Algeria (ICWEAA).

Ansari, N. (2019). *3D Design and Simulation Methods for the Development of Wingsuits*. TUDpress.

Ansari, N., Krzywinski, S., & Frohlich, J. (2018). Towards a combined CAD and CFD development process of a wingsuit. *Multidisciplinary Digital Publishing Institute Proceedings*, 2(6), 228. https://doi.org/10.3390/proceedings2060228

Barlow, J. B., Rae, W. H., & Pope, A. (1999). *Low-speed wind tunnel testing*. John Wiley & Sons.

Chaisson, T., Lee, S., & Burns, D. E. (2022). Design optimization of a wind tunnel force balance using stepwise response surface method. *Journal of Mechanical Science and Technology*, 36(6), 3071-3079. https://doi.org/10.1007/s12206-022-0537-4

Clarke, A., & Gutman, P. O. (2017). Modelling and control of a virtual skydiver. *IFAC-PapersOnLine*, 50(1), 369-374. https://doi.org/10.1016/j.ifacol.2017.08.160

Dvořák, R. (2016). *Aerodynamics of bird flight*. EPJ Web of Conferences,

Feletti, F., Westman, A., & Mei-Dan, O. (2017). *BASE jumping and wingsuit flying injuries*. Extreme Sports Medicine. Springer.

Hayes, S. G., & Venkatraman, P. (2018). *Materials and technology for sportswear and performance apparel*. CRC Press.

Ishikura, K., Yoshimi, J., Matsuda, A., Yamashita, K., Katsu, M., Otsuka, S., & Tkakagi, H. (2014). Influence of a newly-developed triathlon suit on the passive drag and body position. *Procedia*

Engineering, 72, 338-343. https://doi.org/10.1016/j.proeng.2014.06.059

Jacob, J. D., Smith, S. W., Cadogan, D., & Scarborough, S. (2007). *Expanding the small UAV design space with inflatable wings* (0148-7191).

Jun, S., Jeon, Y.-H., Rho, J., & Lee, D. H. (2006). Application of collaborative optimization using genetic algorithm and response surface method to an aircraft wing design. *Journal of Mechanical Science and Technology*, 20, 133-146. https://doi.org/10.1007/s12206-013-0853-9

Kim, M. J., Hwang, H. G., Lee, J. H., Kim, J., Park, J., & Song, G. (2022). Aerodynamic design optimization for a canopy based on response surface methodology and a multi-objective genetic algorithm. *Journal of Mechanical Science and Technology*, 36(9), 4509-4522. https://doi.org/10.1007/s12206-022-0815-1

Kornilovich, A., & Kuzmichev, V. (2016). *development of the design principles of parachute-sports costumes*. Technology of the Textile Industry.

Kornilovich. (2017). *Development of a parachuting suit design process* Anastasia Viktorovna Kornilovich. Ivanovo: IVGPU, 2017].

Merkin, D. (1980). Introduction to the mechanics of a flexible thread. *Science*, 240.

Omholt, S. (2011). *CFD Modeling of a Wingsuit Institutt.* Master's thesis, Institutt for energi-og prosessteknikk.

Ozkan, M. (2022). *Active and passive flow control methods over airfoils for improvement in aerodynamic performance.* New Frontiers in Sustainable Aviation. Springer International Publishing.

Robson, G., & D'Andrea, R. (2010*). Longitudinal stability analysis of a jet-powered wingsuit*. AIAA Atmospheric Flight Mechanics Conference.

Rumsey, C. L. (2016). Turbulence Model Verification and Validation. In *ASME Verification and Validation Symposium* 2016 May 16 (No. NF1676L-22545).

Sestak, T. A. (2017). The effect of surface materials and morphology on wingsuit aerodynamics.

Sieker, J. W., Castillo, E. M., & Vilke, G. M. (2019). Timing of fatal BASE jumping incidents: 1981–2018. *Journal of Forensic and Legal Medicine*, 65, 39-44. https://doi.org/10.1016/j.jflm.2019.04.011

Stockl, A., Sieker, J., Westman, A., & Mei-Dan, O. (2020). Practical and conceptual analysis of wingsuit base flight. *Muscle Ligaments and Tendons Journal*, 10(02). https://doi.org/10.32098/mltj.02.2020.10

Subramanya, S. (2022). A PANS implementation of k-omega SST turbulence model.

Zhang, X. (2016). Flight simulation and stability control of wingsuits. *Georgia Institute of Technology*.